

Dynamical Conductivity Engineering of Graphene Microstrip Patch Ultrawide Band Antennas for THz Communications

Mojtaba Dashti[†] and J David Carey^{,†,‡}*

[†] Department of Electrical and Electronic Engineering, University of Surrey, Guildford, GU2 7XH, United Kingdom

[‡] Advanced Technology Institute, University of Surrey, Guildford, GU2 7XH, United Kingdom

KEYWORDS: dynamical conductivity, graphene antennas, ultrawide band antennas, dielectric constant, THz communications, modeling

ABSTRACT: Future generation local communication systems will need to employ THz frequency bands capable of transferring sizable amounts of data. Current THz technology is limited by upper limits of device cutoff frequencies via electrical excitation and by the lower limits of optical transitions in low dimension quantum structures. Current metallic antennas operating at THz frequencies require high power to overcome scattering losses and tend to have low antenna efficiency. We show here that graphene can sustain electromagnetic propagation at THz frequencies via engineering the intra- and interband contributions to the dynamical

conductivity to produce a variable surface impedance microstrip antenna with a several hundred GHz bandwidth. We report the optimization of a circular graphene microstrip patch antenna on silicon with an optimized return loss of -26 dB, a -10 dB bandwidth of 504 GHz and an antenna efficiency of -3.4 dB operating at a frequency of 2 THz. An improved antenna efficiency of -0.36 dB can be found at 3.5 THz but is accompanied by a lower bandwidth of about 200 GHz. Such large bandwidths and antenna efficiencies offers significant hope for a graphene based flexible and conformal directional antennas that can be employed for future THz local device-to-device communications not currently available.

1. INTRODUCTION

Bridging the THz gap between the highest frequencies of electronics and the lowest frequencies of photonics is one of the ongoing challenges facing electronic and photonic materials and device engineering.^{1,2} Advances in wireless communications are predicted to see global internet protocol (IP) traffic rise from 122 exabytes (10^{18} bytes) per month in 2017 to 278 exabytes per month by 2021, with traffic from wireless and mobile devices predicted by then to account for more than 63% of total IP traffic.³ Channel capacity of 100 Gbit/s will be required for the next generation of communication systems and will require ever increasing bandwidth which in turn encourages exploitation of higher frequency bands, including THz bands, for data transfer.² Knowing that signal attenuation via atmospheric water and molecular absorption is significant at THz frequencies, practical data transmission at these frequencies will mainly involve near field communications, such as device-to-device for wireless personal area networks. Losses above frequencies of 1 THz typically arise from a broad background attenuation of 100 dB/km with levels of signal attenuation peaking at 10^4 dB/km.² Efforts to increase current gain, f_T , or power gain, f_{max} , cutoff frequencies of high electron mobility transistors (HEMTs)

fabricated from Si, SiGe and III-V semiconductors are limited to several hundred GHz,⁴ though an InGaAs channel based metamorphic HEMT was reported as having a f_T of 515 GHz.⁵ Furthermore electrical excitation up to 1 THz using resonant tunnel diodes tends to suffer from low efficiency due to mobility limiting carrier transit times and overall device capacitance. The reduction of the frequencies of optical transitions found in semiconductor lasers below 30 THz (equivalent to transitions with wavelengths beyond 10 μm) remains challenging though free electron laser sources can generate THz radiation but are both bulky and expensive. Power output from even high efficiency quantum cascade lasers also rarely exceed 10 mW under continuous operation at room temperature.⁶ Opportunities therefore to fabricate efficient THz sources, modulators and detectors would open potential new applications in portable imaging for defense and security technologies⁷, in reflectometry-based medical imaging⁸, and in non-destructive ultrafast spectroscopy of materials.⁹ Connected, autonomous and/or smart devices that make use Internet of Things applications will also benefit from the increase in bandwidth for data transfer.¹⁰ Key to these developments is the exploration of the characteristics of new materials and devices at high frequencies. Evaluation of the electrical and electronic properties of graphene for THz applications and in particular for antennas, is the goal of this study. The interest in the use of graphene as a material for THz applications arises from rapid advancements in large-area high-quality production, improvements in carrier mobility potentially resulting in high cutoff frequencies for electrical excitation, and a largely wavelength-independent adsorption for efficient optical detection.^{11,12}

Fabrication of graphene devices that operate at THz frequencies is attractive as the linear low energy band dispersion around the Dirac point results in quasi-particles propagating at Fermi velocities of about 10^6 m/s ($\sim c/300$, where c is the speed of light in vacuum).¹³ The carrier

density can be adjusted by means of the variation of a gate voltage for graphene fabricated in a transistor geometry,¹⁴ or through selective *n*- or *p*-type molecular doping with high charge transfer per molecule¹⁵ both methods resulting in variable conductivity materials for antenna arrays. High carrier mobility graphene devices of tailored geometries on selected substrates can now be regularly fabricated. Another advantage of graphene is the opportunity of tunable plasmon formation at much lower energies than that found via optical excitation of noble metals. Furthermore such graphene plasmons possess a high degree of confinement with lifetimes that extend beyond many hundreds of optical cycles.¹⁶ This has led to the successful development of large area graphene based plasmonic antenna arrays with a signal-to-noise ratio in excess of 100 dB.¹⁷ Choosing the correct graphene-substrate geometry can also lead to a high degree of confinement in a neighboring frequency selective surface resulting in high modulation depth with a low insertion loss for THz modulators.¹⁸ Graphene based split-ring resonator structures can also be engineered to control the inductive currents flowing in the split-ring elements, and in the capacitive elements to maximize the strength of the electromagnetic field in the gap between the arms; this has led to the development of a low bias (0.5 V) modulator operating between 2 and 3 THz.¹⁹ Conventional metal antennas fabricated at micron scales tend to have operating frequencies at hundreds of THz. At these very high frequencies, high power is often required to overcome scattering losses in the metal and propagation losses in the atmosphere which limits their range for data transfer. Antennas operating at THz frequencies have the significant advantage of potentially higher bandwidth for data transfer with improved resolution and spatial directivity. Graphene based antennas, as an alternative to metal antennas, have been far less explored as the sizes of graphene samples were previously limited but this is less of a concern with wafer scale production possible via CVD and related methods.^{20,21} The development of

wafer-scale production of graphene has already seen significant developments with, for example, a 50 GBit/s graphene photodetector integrated into a silicon photonic communication system.²² Large area graphene can also be placed on conformal surfaces, such as windows to act as electrochromic devices.

Key to many of these applications is the opportunity to make use of graphene as a conductive, flexible and light weight material which can be produced by technology-mature, wafer-scale production methods, and which is compatible with microwave device processing.^{22,23} Critical evaluation of graphene as a potential new material for high frequency applications therefore requires determination of the dynamical conductivity response and how parameters such as the carrier density and carrier scattering time affect the real and imaginary components of both the 2D conductivity and the dielectric constant. Knowledge of these parameters as well as the dielectric environment e.g. choice of substrate, can then be fed into the design of a microstrip graphene patch antenna. A microstrip antenna architecture is employed as such antennas are of smaller physical size compared to dipole, Yagi-Uda or horn antennas and can be patterned on non-planar surfaces while remaining conformal with graphene. The microstrip antenna can also be easily designed to produce variety of radiation patterns and polarization and depending on shape (circular, rectangular etc.), and can have dual or multi-frequency operation. The principal disadvantage of microstrip antennas, however, tends to be lower gain compared to other types of antenna design and a narrower bandwidth. We will show here that graphene based antennas can actually support a large bandwidth without significantly comprising antenna efficiency.

We first calculate, within the random phase approximation, the dynamical conductivity response and relative dielectric constant of graphene taking into account both the intra- and interband contributions to conductivity in the $q \rightarrow 0$ local limit. We further identify the factors

that influence the characteristics of a circular microstrip antenna including choice of dielectric substrate, resonant frequency and bandwidth response of the return loss in the 1-10 THz frequency range. Finally, we calculate the antenna properties such as voltage standing wave ratio, radiation efficiency, and the radiation pattern of both the electric and magnetic field components. The broader prospects for graphene based antennas operating in the THz part of the spectrum are also discussed.

2. DYNAMICAL CONDUCTIVITY IN GRAPHENE

The dynamical sheet conductivity, $\sigma(q, \omega)$, is the linear response of the current density to an applied time-varying electric field. The $q \rightarrow 0$ in-plane wavevector limit of $\sigma(q, \omega)$ describes the response to electromagnetic waves whose wavelengths are longer than the characteristic length scale found in electronic systems. Within the random phase approximation the dynamical sheet conductivity, in the local limit, can be expressed as^{24,25}

$$\sigma_s(\omega) = \frac{2ie^2 k_B T}{\pi \hbar^2 (\omega + i/\tau)} \ln \left(2 \cosh \frac{E_F}{2k_B T} \right) + \frac{e^2}{4\hbar} \left(\frac{1}{2} + \frac{1}{\pi} \tan^{-1} \left(\frac{\hbar \omega - 2E_F}{2k_B T} \right) \right) - \frac{i}{2\pi} \ln \left(\frac{(\hbar \omega + 2E_F)^2}{(\hbar \omega - 2E_F)^2 + 4(k_B T)^2} \right) \quad (1)$$

where k_B is Boltzmann's constant, τ is the carrier scattering time, T is temperature, ω is frequency and E_F is the Fermi energy. The Fermi energy can be related to the net carrier density, assuming a linear low energy density of states near the Dirac point, via the equation $E_F = \hbar v_F \sqrt{n\pi}$. For a Fermi velocity of 10^6 m/s and a carrier density, n , measured in cm^{-2} , the value of E_F , measured in eV, can be approximated to be $E_F(\text{eV}) = 1.166 \times 10^{-7} \sqrt{n(\text{cm}^{-2})}$. The first term in equation (1) is associated with intraband conductivity and the second with the

interband conductivity, as shown in **Figure 1(a)**. For doped graphene, interband transitions can only occur for $\hbar\omega > 2|E_F|$ to account for Pauli state blocking (green line, Figure 1(a)).

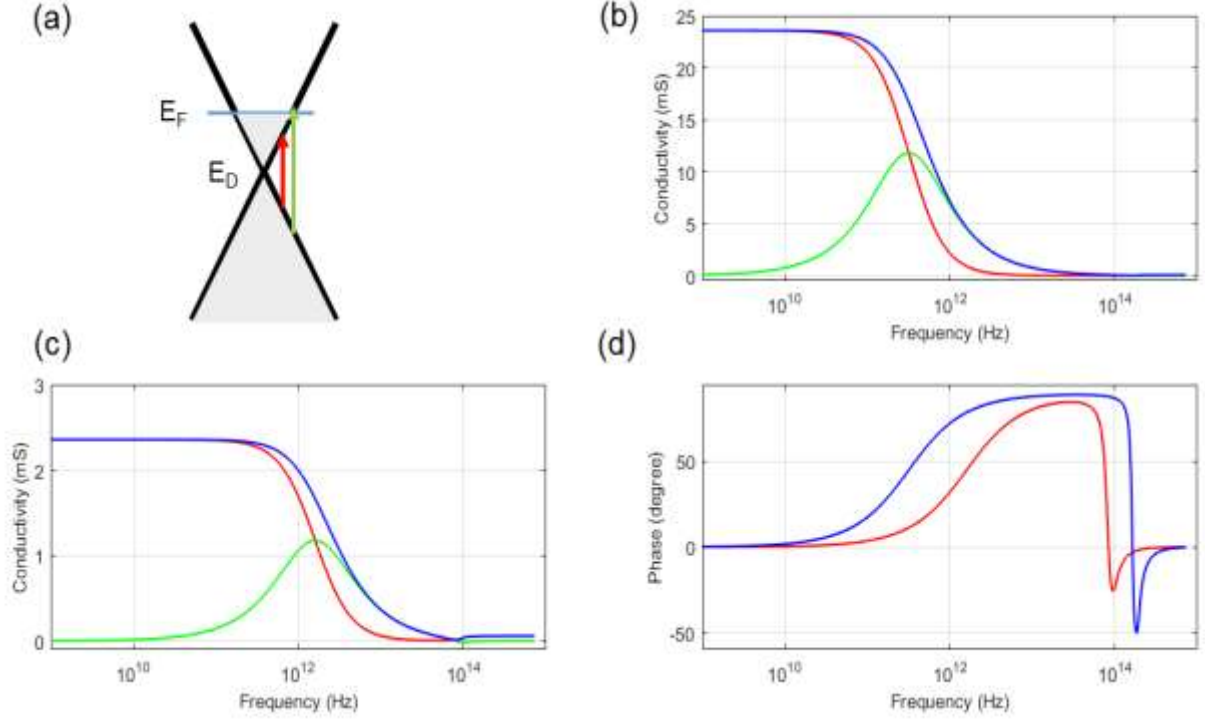


Figure 1 (a) Schematic of the low energy band dispersion of graphene around the Dirac point, E_D , showing the allowed (green line) and Pauli forbidden (red line) interband transitions for the case of n -doped graphene where the Fermi energy, E_F , is above the Dirac point. **(b)** Variation of the magnitude (blue curve), and the real (red curve) and imaginary (green curve) components of the dynamical conductivity with frequency for graphene with an electron concentration of $1.2 \times 10^{13} \text{ cm}^{-2}$ and scattering time of 0.5 ps at 293 K. **(c)** Variation of the magnitude (blue curve), and the real (red curve) and imaginary (green curve) components of the dynamical conductivity with frequency for graphene with an electron concentration of $2.9 \times 10^{12} \text{ cm}^{-2}$ and scattering time of 0.1 ps at 293 K. **(d)** Relative phase between the real and imaginary components of conductivity for the data presented in (b) above (blue curve) and in (c) above (red curve) as a function of frequency.

The variation of the magnitude of graphene conductivity, as calculated using equation (1) at 293 K, along with real and imaginary components, for a higher quality doped graphene with an electron concentration of $1.2 \times 10^{13} \text{ cm}^{-2}$, corresponding to a Fermi energy of about 0.4 eV above E_D , and at a scattering time of 0.5 ps, is shown in **Figure 1(b)**. For a relatively poorer graphene sample with lower doping of $2.9 \times 10^{12} \text{ cm}^{-2}$, (Fermi energy of about 0.2 eV above E_D) and a shorter scattering time of 0.1 ps, the variation of the conductivity with frequency is shown in **Figure 1(c)**. In both cases at low frequencies, where $\omega\tau \ll 1$, there is no contribution from interband conductivity due to Pauli state blocking and the magnitude of the conductivity is determined by the real component of the intraband conduction, which takes the simplified form $\text{Re } \sigma_{s,\text{intra}} = \frac{e^2 E_F \tau}{\pi \hbar^2}$. For E_F measured in eV and τ measured in ps, this simplifies to $\text{Re } \sigma_{s,\text{intra}} = 0.118 E_F (\text{eV}) \tau (\text{ps})$; for the cases considered in Figure 1(b) and (c) the low frequency conductivity is 24 mS and 2.4 mS, respectively. At such low frequencies (from DC up to around 10 GHz) the conductivity exhibits a dispersionless behavior which could be useful for broadband applications such as half-wavelength filters or quarter-wavelength couplers. The frequency-independent behavior of the conductivity at frequencies up to 10 GHz can be compared with conventional metals where the current flow arising from an incident EM wave is constrained to about five skin depths from the surface. As the frequency increases, surface roughness losses in a metal play an ever increasing role with a typical loss rate of 0.1 dB/mm per GHz frequency reported for mm-long coplanar waveguide (CPW) structures fabricated from either micron-size or nanometer-size grains of silver.²⁶ Skulason *et al.* have reported that measurements made on CVD grown graphene fabricated in a CPW structure also reveal a negligible dependence on frequency up to 110 GHz, which was attributed to a negligible influence of the skin effect and an insignificant contribution from the kinetic inductance.²⁷ A dispersionless behavior in the high

frequency transport behavior of multiwalled carbon nanotube–polymer composite CPWs with losses as low as 0.15 dB/mm between 40 and 110 GHz has also been reported.²⁸ In this case the frequency-independent behavior was attributed to the capacitive coupling between the nanotubes surrounded by a thin polymer layer coating when the nanotube volume fraction exceeds the percolation threshold.

As the frequency increases the imaginary components in Figure 1(b) and (c) increase reaching a maximum contribution when $\omega\tau = 1$, displaying a Drude-type behavior. At this frequency, the real and imaginary components of the conductivity have the same magnitude, $\frac{e^2 E_F \tau}{2\pi\hbar^2}$, being half that found for the real component at low frequencies; there is negligible contribution from interband transitions to the conduction at this frequency. Analysis of the relative phase between the real and imaginary components of the conductivity shows **(Figure 1(d))** that initially at low frequencies (below 10-20 GHz) that the real and imaginary component are in phase with each other. Above 10-20 GHz the phase begins to take a positive value indicative of the phase developing an inductive contribution to the conductivity. At higher frequencies the conductivity decreases as ohmic conduction losses increase as $\omega \sim 1/\tau$, and when $\omega\tau \gg 1$ the conductivity has contributions from both intra- and interband conduction. In this high frequency regime **(Figure 2(a) and (b))** the real component of the interband conductivity, $\text{Re } \sigma_{s,\text{inter}}$, is given by

$$\text{Re } \sigma_{s,\text{inter}} = \frac{e^2}{4\hbar} \left(\frac{1}{2} + \frac{1}{\pi} \tan^{-1} \left(\frac{\hbar\omega - 2E_F}{2k_B T} \right) \right). \quad (2)$$

When $\hbar\omega - 2E_F \gg k_B T$, this reduces to the limiting value of $\text{Re } \sigma_{s,\text{inter}} \rightarrow e^2/4\hbar$ or $\pi e^2/2h = 6.09 \times 10^{-2}$ mS. This leveling out of conductivity has recently been seen in the THz and mid IR reflectance of graphene grown on SiC.²⁹ The increase in the real component of the conductivity

to the saturating value occurs at about $2E_F$ in both cases of Figure 2(a) and (b) reflecting the onset of interband absorption from occupied to unoccupied states overcoming Pauli blocking.

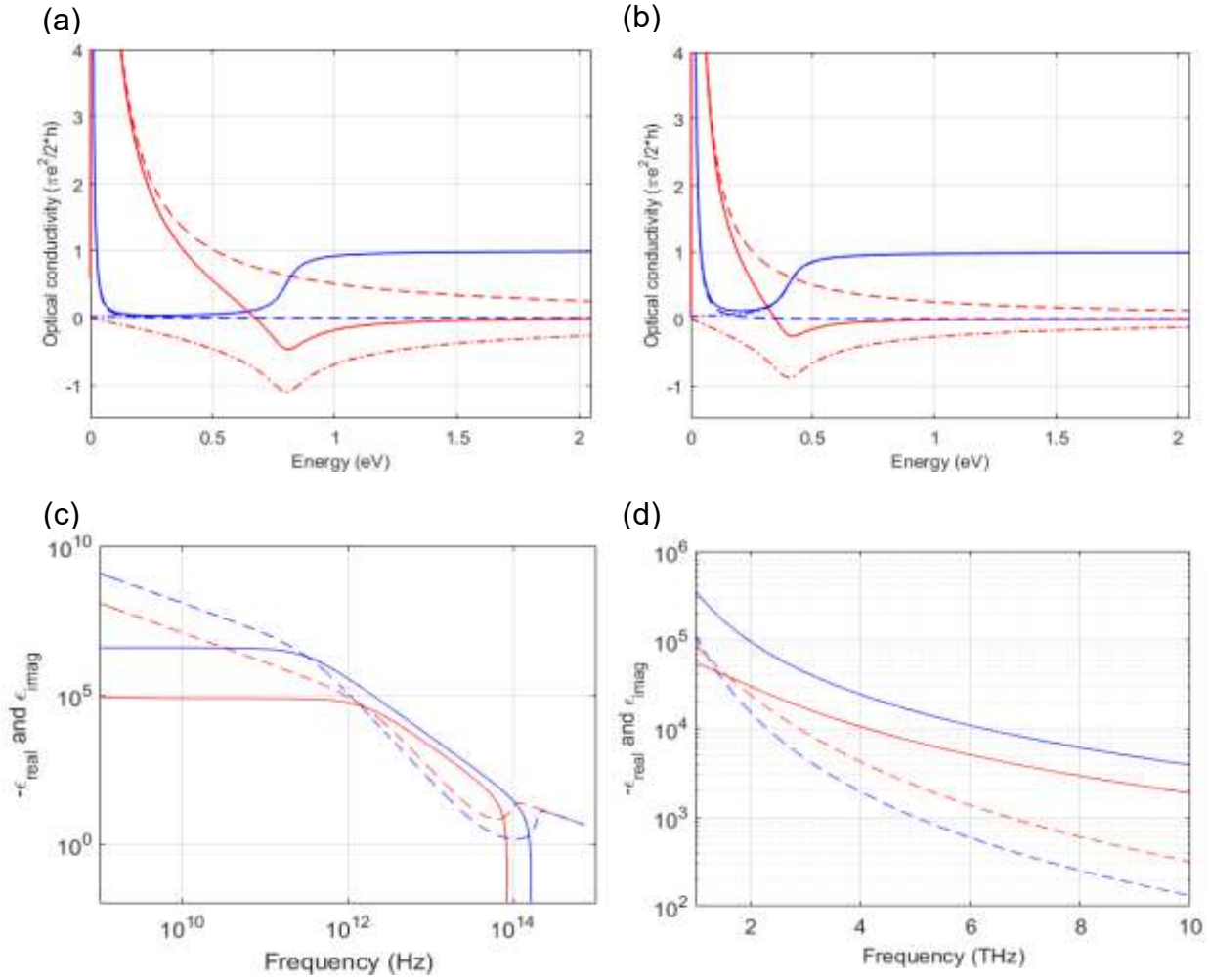


Figure 2 Variation of the total real (blue curve) and total imaginary (red curve) parts of the dynamical conductivity with frequency where the dashed lines (—) show the contribution from the intraband conduction and the dashed-dot lines (— ·) show the contribution from the interband conduction. The conductivity is plotted in units of $\pi e^2/2h$ for a graphene sample with (a) an electron concentration of $1.2 \times 10^{13} \text{ cm}^{-2}$ and scattering time of 0.5 ps and (b) electron concentration of $2.9 \times 10^{12} \text{ cm}^{-2}$ and scattering time of 0.1 ps at 293 K. (c) Variation of magnitude of the real (solid curve) and the imaginary components (dashed curves) of the relative dielectric constant with frequency for the sample described in (a) (blue curves) and the sample described in (b) (red curves). (d) As figure (c) but in the 1 - 10 THz frequency range.

The imaginary component of the conductivity has competing contributions from the (positive) intraband and (negative) interband conduction. At these high energies the relative phase (Figure 1(d)) between the real and imaginary conduction changes rapidly becoming negative over a narrow range of energy signifying the presence of a more prominent capacitive component in conduction. Finally, the high frequency dielectric properties of graphene can be expressed as

$\tilde{\epsilon} = \epsilon_r \epsilon_0 = \epsilon_0 \left(1 + \frac{i\sigma_s(\omega)}{\epsilon_0 \omega t_g} \right)$, where t_g is the thickness of graphene (0.345 nm). Separating out the

real and imaginary components, $\epsilon_r = \epsilon_1 + i\epsilon_2$, gives

$$\epsilon_1 = \left(1 - \frac{\sigma_{imag}}{\epsilon_0 \omega t_g} \right) \text{ and } \epsilon_2 = \frac{\sigma_{rl}}{\epsilon_0 \omega t_g}. \quad (3)$$

For the typical frequencies considered here the values of ϵ_1 are negative, as a result the magnitude of the real component and the imaginary component can be plotted conveniently together, **Figure 2 (c) and (d)**. As can be seen the value of ϵ_1 is negative indicating metallic like behavior and that above 1 THz the magnitude of ϵ_2 is less than of ϵ_1 however below 1 THz, the magnitude of ϵ_1 ends to levels out down frequencies around 1 GHz. Having explored the dynamic conductivity we move to calculation of the THz properties of a graphene antenna.

3. GRAPHENE ANTENNA DESIGN

3.1 Patch antenna design considerations

Graphene antenna design calculations were performed using a commercial electromagnetic simulator, CST STUDIO SUITE (version 2015).³⁰ Within CST STUDIO SUITE, graphene is described by the selectable values of the real and imaginary components of the dielectric constant along with a relative permeability equal to 1. An unintentionally doped graphene layer

is simulated at 293 K with a scattering time of 0.1 ps. A circular microstrip antenna of radius a lying on a substrate of length L_s and thickness h_s with relative substrate dielectric constant ϵ_r was modelled, **Figure 3(a)**.

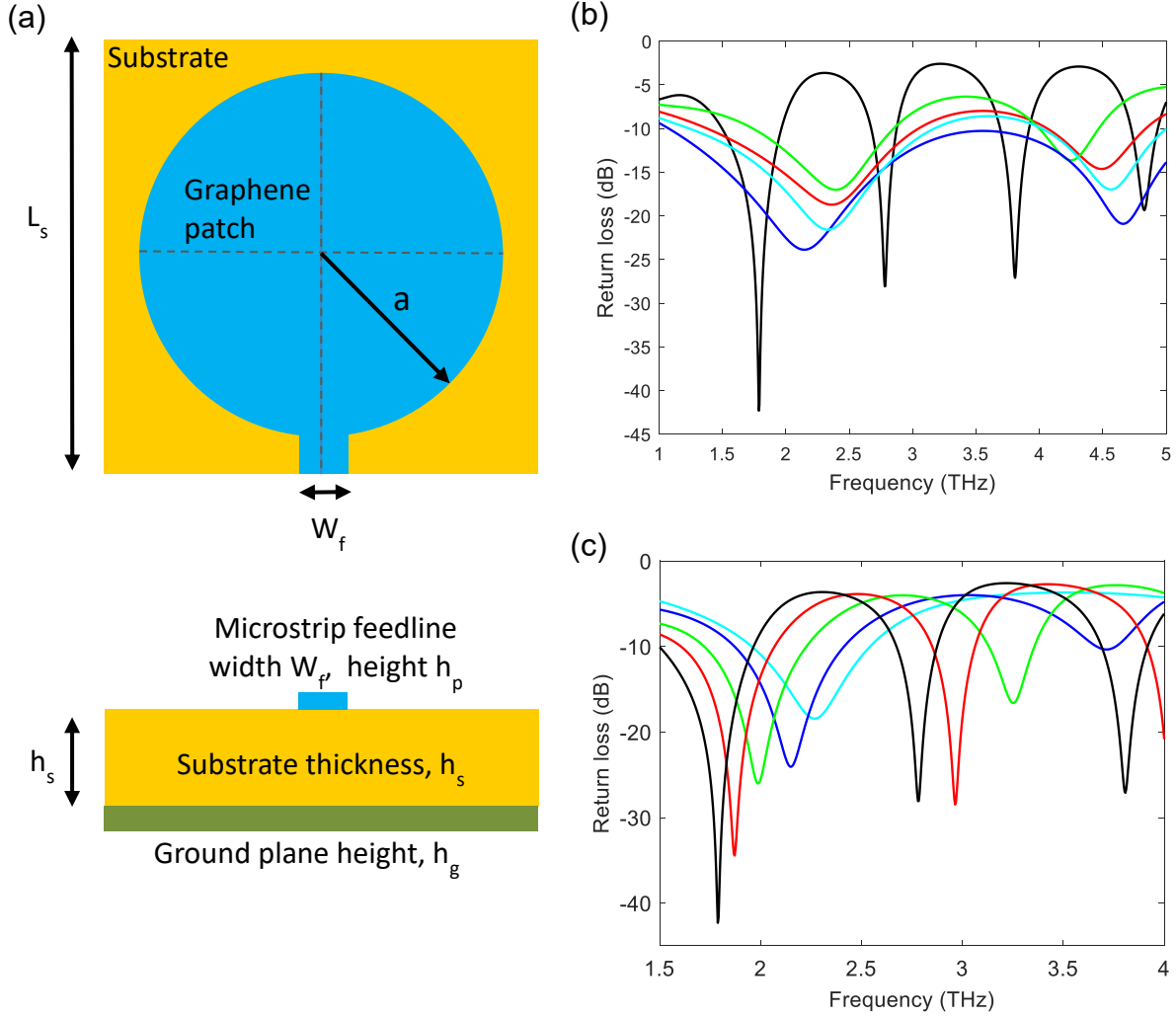


Figure 3 (a) Geometry of the circular graphene patch antenna of radius a lying on a substrate of side length L_s , and microstrip feedline of width W_f . The thickness of the substrate is labelled h_s . **(b)** Variation of return loss for a graphene circular patch antenna of radius $18 \mu\text{m}$ on silicon ($\epsilon_r = 11.9$, black curve), polyimide ($\epsilon_r = 3.5$, dark blue curve), quartz ($\epsilon_r = 3.75$, cyan curve), FR4 ($\epsilon_r = 4.3$, red curve), glass ($\epsilon_r = 4.82$, green), and substrates each of thickness $10 \mu\text{m}$. **(c)** Variation of return loss for a graphene circular patch antenna of radius $18 \mu\text{m}$ on silicon for substrate thickness for $10 \mu\text{m}$ (black curve), $8 \mu\text{m}$ (red curve), $6 \mu\text{m}$ (green curve), $4 \mu\text{m}$ (purple curve) and $2 \mu\text{m}$ (cyan curve).

A microstrip feeding technique with centre feed of width W_f and height h_p , is employed in this design excite the antenna; the height of the ground plane is h_g . The resonant frequency, return loss (RL) and -10 dB RL bandwidth of the antenna depend on these parameters. With a large parameter space to explore we note to a first approximation that the resonant antenna frequency depends on the radius of the circular patch via equation 4a

$$f_r = \frac{1}{2\pi\sqrt{\mu\epsilon}} \left(\frac{X'_{mn}}{a} \right) \quad (4a)$$

where X'_{mn} is the represents the zeros of the Bessel's function.³¹ For the lowest mode,

$X'_{11} = 1.8414$ and the resonant frequency of equation 4a reduces to

$$f_r = \frac{1.8414c}{2\pi a\sqrt{\epsilon_r}}. \quad (4b)$$

The effects of fringing fields on the resonant frequency are not taken into account by equation 4b; consideration of the fringing effect is important as it makes the patch appear to be electrically larger. Fringing effects can be taken into account by replacing a by an effective radius, a_{eff} , via equation 5

$$a_{eff} = a \left\{ 1 + \frac{2h}{a\pi\epsilon_r} \left(\ln \left(\frac{a\pi}{2h_s} \right) + 1.7726 \right) \right\}^{1/2} \quad (5)$$

With the aid of equations (4b) and (5) and for the lowest resonant frequency of about 2 THz, the radius of the antenna found is calculated to be 18 μm on a silicon substrate. We show below how the choice of substrate material and dimensions affect the RL and other parameters. With a graphene antenna radius of 18 μm the substrate size is fixed as 40 μm x 40 μm , as shown in figure 3a.

3.2 Patch antenna substrate design considerations

The selection of the antenna's substrate is important as it not only does it provide mechanical support but a different substrate dielectric constant affects the field distribution which in turn influences the antenna's radiation characteristics. We have explored the graphene patch antenna characteristics on selected substrates of silicon ($\epsilon_r = 11.9$), FR4 ($\epsilon_r = 4.3$), glass ($\epsilon_r = 4.82$), polyimide ($\epsilon_r = 3.5$) and quartz ($\epsilon_r = 3.75$). **Figure 3b** shows the return loss has a number of resonances corresponding to the successive zeros of the Bessel function. The largest (most negative) RL occurs for the case of a silicon substrate with a RL of -42.3 dB at a frequency of 1.79 THz with a -10 dB RL bandwidth of 464 GHz. For graphene on Si there are two further resonances at 2.78 and 3.81 THz with bandwidths of 200 and 228 GHz, respectively. For the cases of graphene on the other substrates the values of return loss are lower (less negative) never going below -23 dB; these calculations were done for a substrate thickness of 10 μm . As a Si substrate appears to give the largest RL we have further explored the effect of different silicon substrate thicknesses (**Figure 3(c)**) between 2 to 10 μm . The value of RL becomes larger for thicker substrates though the value of -10 dB bandwidth decreases for increasing thickness. For example, for if a resonant frequency of 2 THz is required a Si substrate of 6 μm thickness should be used where the RL is -26.0 dB and the -10 dB RL bandwidth is 500 GHz. The values of the RL and ultra-wide bandwidth found here can be compared with, for example, Thampy *et al.* who fabricated a rectangular patch antenna on a polyimide substrate operating at 6 THz.³² They found a -40 dB return loss with a -10 dB bandwidth of 180 GHz, smaller than that found here. Bala and Marwaha explored the characteristics of a triangular graphene antenna of 40 μm side on quartz on SiO_2 designed to operate between 1-3 THz.³³ They reported a gate tunable return loss which was maximized at -17.3 dB at a frequency of 2.4 THz.

3.3 Patch antenna performance characteristics

One of the key performance indicators for an antenna is the voltage standing wave ratio (VSWR), which is the ratio of maximum voltage amplitude of a standing wave to the minimum voltage amplitude. A VSWR below 2.0 corresponds to a reflection coefficient of 1/3 with the reflected power being -9.55 dB; a VSWR below 2.0 is taken as a good antenna matching. **Figure 4(a)** is the calculated VSWR for an 18 μm radius graphene patch antenna with a 6 μm wide feedline on a 6 μm thickness Si substrate of length 40 μm . Between 1.70 and 2.24 THz the VSWR is below 2.0 corresponding to the first resonance at about 2 THz. A second acceptable range of values of the VSWR is found between 3.12 and 3.36 THz, and a third range is between 4.27 and 4.52 THz. It is also possible to determine the field distributions and antenna efficiency at the different resonant frequencies. For the case of the resonance at 2 THz, **Figure 4(b) - (c)** shows a main lobe of magnitude of 4.7 dBi with main lobe direction of 107° . The angular width (measured at 3 dB) is 121° and a side lobe with a magnitude of -5.8 dB is also found. The graphene patch antenna at 2 THz had a directivity of 4.7 dBi with an antenna radiation efficiency of -3.4 dB and the total efficiency of -4.2 dB, (**Figure 4(d)**).

The results of the VSWR calculations show that the graphene antenna has two further resonances worth exploring despite lower -10 dB RL bandwidths. The radiation pattern of the graphene patch antenna at 3.25 THz, **Figure 5(a) and (b)**, is tilted by 99° downward from the broadside direction (direction perpendicular to the patch). A main lobe magnitude of 6.5 dBi, main lobe direction of 99° , angular width (3 dB) of 80.1° with a side lobe level of -13.5 dB is obtained. The graphene patch antenna had a directivity of 6.5 dBi, antenna efficiency of -1.01 dB and total efficiency of -1.56 dB at 3.25 THz.

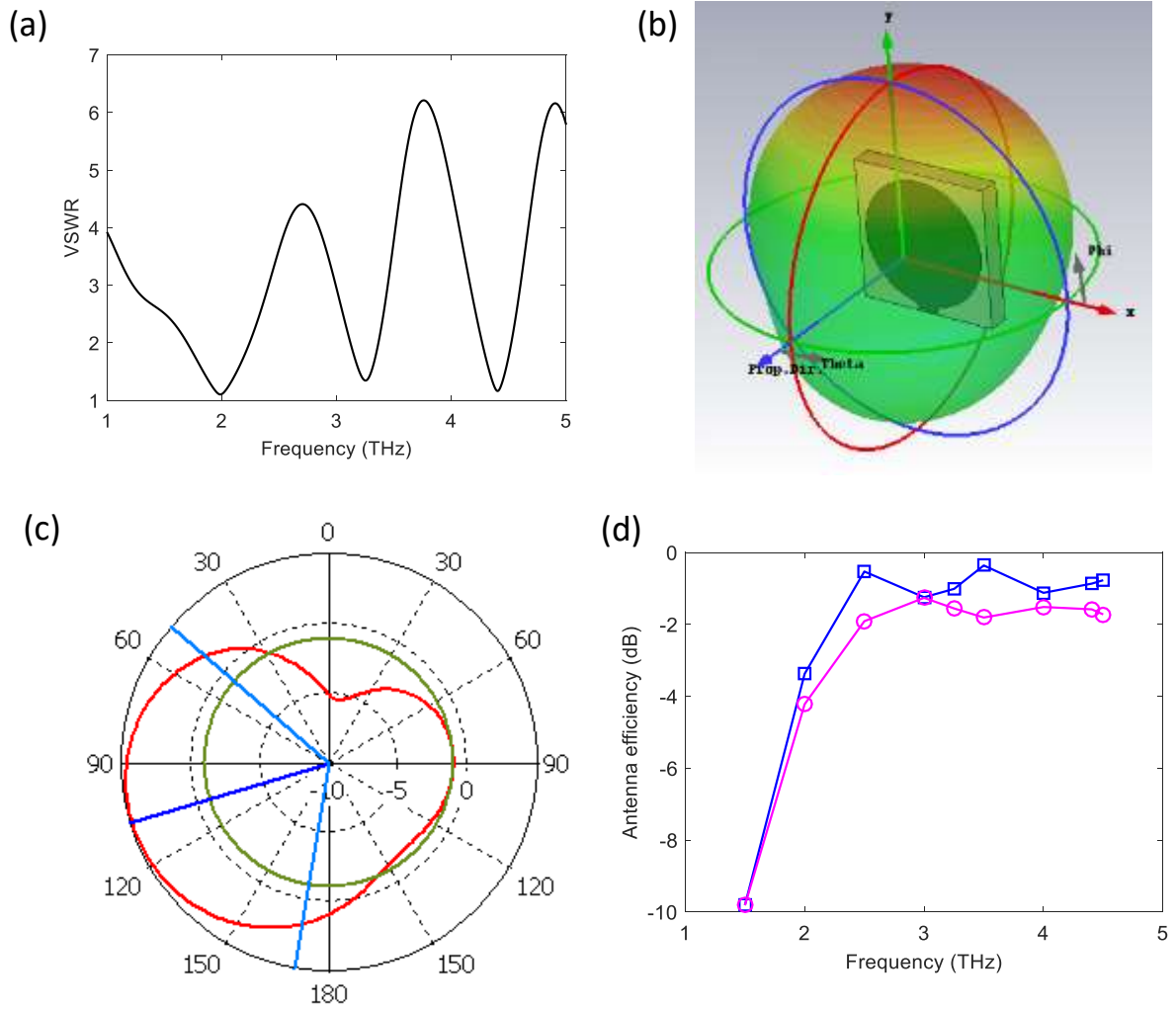


Figure 4 (a) Variation of antenna voltage standing wave (VSWR) ratio for a circular graphene patch antenna of radius $18 \mu\text{m}$ lying on a silicon substrate of side length $40 \mu\text{m}$, microstrip feedline of width $6 \mu\text{m}$ and thickness of Si substrate of $6 \mu\text{m}$. (b) 3D directivity and (c) polar 2D antenna radiation pattern (units: degrees and dBi) where the red line is the electric field and the green line is the magnetic field at 2 THz. (d) Variation of the antenna radiation efficiency (blue curve) and total efficiency (pink curve) for the antenna described in part (a) as a function of frequency.

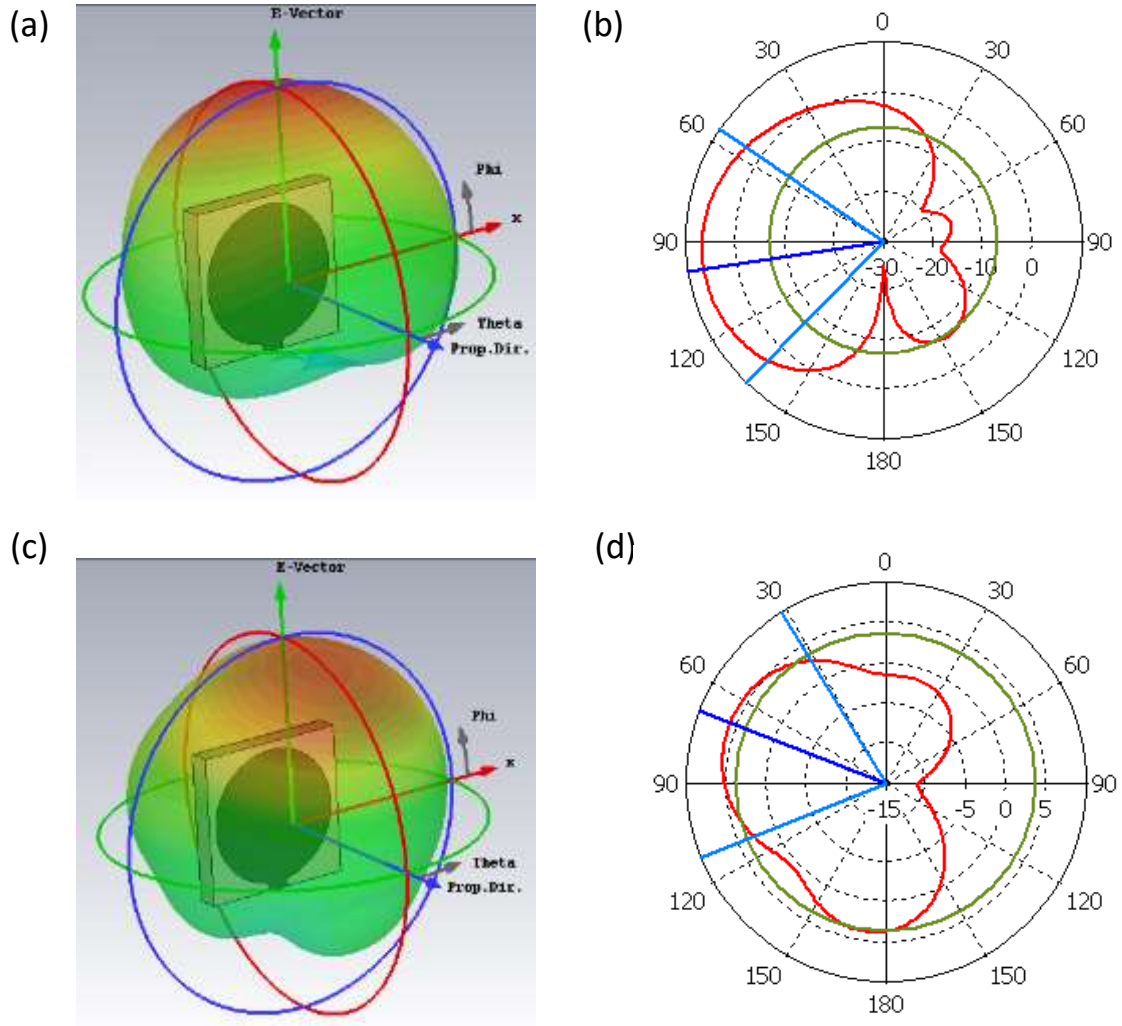


Figure 5 (a) 3D radiation pattern and (b) polar 2D radiation pattern (units: degrees and dBi) where the red line is the electric field and the green line is the magnetic field at 3.25 THz. (c) 3D radiation pattern and (d) polar 2D radiation pattern (units: degrees and dBi) where the red line is the electric field and the green line is the magnetic field at 4.40 THz.

From **Figure 5(c)** and **(d)** it is observed that the radiation pattern of the graphene patch antenna at 4.40 THz is tilted by 69° downward from the broadside direction. A main lobe magnitude of

5.78 dBi, main lobe direction of 69° , angular width (3 dB) of 80.4° and a side lobe level of -2 dB is found in this case. The graphene patch antenna had a directivity of 5.78 dBi, radiation antenna efficiency of -0.87 dB and total efficiency of -1.58 dB at a frequency of 4.40 THz. The values for radiation and total efficiencies obtained at 4.40 THz are better compared to the values at 2.00 and 3.25 THz with comparatively less beam tilting; Figure 4d shows the antenna radiation efficiency of the graphene patch antenna for different frequencies with the highest radiation efficiency of -0.36 dB is found at 3.5 THz. Figure 4(d) also shows the total radiation efficiency at various frequencies. The total efficiency also considers the effect of the conduction and dielectric losses in the antenna. Similar to the radiation efficiency plot, we can see that the total radiation efficiency for 2 THz is less compared to the other two resonant bands obtained. Here, highest total radiation efficiency is obtained at 3 THz which is -1.26 dB.

4. CONCLUSIONS

We have explored the high frequency conductivity of graphene and the contributions made by intra- and interband transitions to the conductivity in different frequency ranges. We have shown that the dynamical behavior of graphene for frequencies up to about 10 THz shows a largely dispersionless response whose magnitude can be engineered via doping. A circular graphene patch microstrip antenna on Si has been designed and at 2 THz a return loss of -26 dB with a bandwidth of 504 GHz has been calculated. In addition to the desired frequency band, two additional resonant frequency bands centred at 3.25 and 4.40 THz are obtained but with reduced bandwidths of about 200 GHz. The ultrawide bandwidths found here offers the potential for short range THz communications with high data rates based on graphene.

AUTHOR INFORMATION

Corresponding Author

* E-mail: david.carey@surrey.ac.uk

Author Contributions

The manuscript was written through contributions of both authors. Both authors have given approval to the final version of the manuscript.

Notes

The authors declare no competing financial interests. The authors confirm that data underlying the findings are available without restriction. Details of the data and how to request access are available from the University of Surrey Publications Repository.

ACKNOWLEDGMENTS

J.D.C. acknowledges current support for graphene research from EPSRC Grant EP/L02263X/1.

References

- (1) Dhillon, S. S. *et al.* The 2017 Terahertz Science and Technology Roadmap *J. Phys. D: Appl. Phys.* **2017**, 50, 043001.
- (2) Koenig, S.; Lopez-Diaz, D.; Antes, J.; Boes, F.; Henneberger, R.; Leuther, A.; Tessmann, A.; Schmogrow, R.; Hillerkuss, D.; Palmer, R. *et al.* Wireless Sub-THz Communication System With High Data Rate. *Nature Photonics* **2013**, 7, 977-981.
- (3) Cisco Visual Networking Index: Forecast and Methodology, 2016–2021, **June 2017**, 1-17.
- (4) Schwierz, F. Graphene Transistors. *Nature Nanotechnology* **2010**, 5, 487-496.
- (5) Leuther, A.; Tessmann, A.; Dammann, M.; Massler, H. Schlechtweg, M.; Ambacher, O. 35 nm mHEMT Technology for THz and Ultra Low Noise Applications, in: Proc. of International Conference on Indium Phosphide and Related Materials, IPRM, **2013**, pp. 1–2.
- (6) Belkin, M.; Capasso, F. New Frontiers in Quantum Cascade Lasers: High Performance Room Temperature Terahertz Sources. *Physica Scripta* **2015**, 90, 118002.
- (7) Palka, N.; Kowalski, M.; Ryneic, R.; Szustakowski, M.; Czerwinska, E.; THz Screening for Civil and Military Security, Chapter 11 in THz and Security Applications THz and Security Applications: Detectors, Sources and Associated Electronics for THz Applications, Ed. Corsi, C.; Sizov, F. *NATO Science for Peace and Security Series B: Physics and Biophysics*, Springer Netherlands, **2014**.
- (8) Ji, Y.; Oh, S.; Kang, S.; Heo, J.; Kim, S.; Choi, Y.; Song, S.; Son, H.; Kim, S.; Lee, J. *et al.* Terahertz Reflectometry Imaging For Low and High Grade Gliomas. *Scientific Reports* **2016**, 6, 36040.

- (9) McIntosh, A.; Yang, B.; Goldup, S.; Watkinson, M.; Donnan, R. Terahertz Spectroscopy: A Powerful New Tool For The Chemical Sciences? *Chem. Soc. Rev.* **2012**, *41*, 2072-2082.
- (10) Nagatsuma, T.; Ducournau, G.; Renaud, C. Advances in Terahertz Communications Accelerated By Photonics. *Nature Photonics* **2016**, *10*, 371-379.
- (11) Avouris, P. Graphene: Electronic and Photonic Properties and Devices. *Nano Letters* **2010**, *10*, 4285-4294.
- (12) Low, T.; Avouris, P. Graphene Plasmonics for Terahertz to Mid-Infrared Applications. *ACS Nano* **2014**, *8*, 1086-1101.
- (13) Novoselov, K.; Fal'ko, V.; Colombo, L.; Gellert, P.; Schwab, M.; Kim, K. A Roadmap for Graphene. *Nature* **2012**, *490*, 192-200.
- (14) Novoselov, K.; Geim, A. K.; Morozov, S. V.; Jiang, D.; Zhang, Y.; Dubonas, S. V.; Grigorieva, I. V.; Firsov, A. A. Electric Field Effect in Atomically Thin Carbon Films. *Science* **2004**, *306*, 666-669.
- (15) Samuels, A.J.; Carey, J.D. Engineering Graphene Conductivity for Flexible and High-Frequency Applications. *ACS Applied Materials & Interfaces* **2015**, *7*, 22246-22255.
- (16) Koppens, F.; Chang, D.; García de Abajo, F. Graphene Plasmonics: A Platform for Strong Light-Matter Interactions. *Nano Letters* **2011**, *11*, 3370-3377.
- (17) Yardimci, N.; Jarrahi, M. High Sensitivity Terahertz Detection through Large-Area Plasmonic Nano-Antenna Arrays. *Scientific Reports* **2017**, *7*, 42667.
- (18) Yan, R.; Arezoomandan, S.; Sensale-Rodriguez, B.; Xing, H. Exceptional Terahertz Wave Modulation in Graphene Enhanced by Frequency Selective Surfaces. *ACS Photonics* **2016**, *3*, 315-323.

- (19) Degl'Innocenti, R.; Jessop, D.; Shah, Y.; Sibik, J.; Zeitler, J.; Kidambi, P.; Hofmann, S.; Beere, H.; Ritchie, D. Low-Bias Terahertz Amplitude Modulator Based on Split-Ring Resonators and Graphene. *ACS Nano* **2014**, *8*, 2548-2554.
- (20) Reina, A.; Jia, X.; Ho, J.; Nezich, D.; Son, H.; Bulovic, V.; Dresselhaus, M.; Kong, J. Large Area, Few-Layer Graphene Films on Arbitrary Substrates by Chemical Vapor Deposition. *Nano Letters* **2009**, *9*, 30-35.
- (21) Kim, K.; Zhao, Y.; Jang, H.; Lee, S.; Kim, J.; Kim, K.; Ahn, J.; Kim, P.; Choi, J.; Hong, B. Large-Scale Pattern Growth of Graphene Films for Stretchable Transparent Electrodes. *Nature* **2009**, *457*, 706-710.
- (22) Schall, D.; Neumaier, D.; Mohsin, M.; Chmielak, B.; Bolten, J.; Porschatis, C.; Prinzen, A.; Matheisen, C.; Kuebart, W.; Junginger, B. Templ, W.; Giesecke, A.L.; Kurz, H. 50 GBit/s Photodetectors Based on Wafer-Scale Graphene for Integrated Silicon Photonic Communication Systems. *ACS Photonics* **2014**, *1*, 781-784.
- (23) Huang, X.; Leng, T.; Zhu, M.; Zhang, X.; Chen, J.; Chang, K.; Aqeeli, M.; Geim, A.; Novoselov, K.; Hu, Z. Highly Flexible and Conductive Printed Graphene for Wireless Wearable Communications Applications. *Scientific Reports* **2015**, *5*, 18298.
- (24) Falkovsky, L.; Pershoguba, S. Optical Far-Infrared Properties of a Graphene Monolayer and Multilayer. *Physical Review B* **2007**, *76*, 153410.
- (25) Yao, Y.; Kats, M.; Genevet, P.; Yu, N.; Song, Y.; Kong, J.; Capasso, F. Broad Electrical Tuning Of Graphene-Loaded Plasmonic Antennas. *Nano Letters* **2013**, *13*, 1257-1264.
- (26) Alshehri, A.; Jakubowska, M.; Młóżniak, A.; Horaczek, M.; Rudka, D.; Free, C.; Carey, J. Enhanced Electrical Conductivity of Silver Nanoparticles for High Frequency Electronic Applications. *ACS Appl. Mater. Interfaces* **2012**, *4*, 7007-7010.

- (27) Skulason, H.; Nguyen, H.; Guermoune, A.; Sridharan, V.; Siaj, M.; Caloz, C.; Szkopek, T. 110 GHz Measurement of Large-Area Graphene Integrated in Low-Loss Microwave Structures. *Appl. Phys. Lett.* **2011**, 99, 153504.
- (28) Alshehri, A.; Jakubowska, M.; Sloma, M.; Horaczek, M.; Rudka, D.; Free, C.; Carey, J. Electrical Performance of Carbon Nanotube-Polymer Composites at Frequencies up to 220 GHz. *Appl. Phys. Lett.* **2011**, 99, 153109.
- (29) Santos, C.; Joucken, F.; De Sousa Meneses, D.; Echegut, P.; Campos-Delgado, J.; Louette, P.; Raskin, J.; Hackens, B. Terahertz and Mid-Infrared Reflectance of Epitaxial Graphene. *Scientific Reports* **2016**, 6, 24301
- (30) Computer Simulation Technology (CST) STUDIO SUITE, 2015.
- (31) Balanis, C. Antenna Theory. Hoboken, NJ: Wiley Interscience, 2005.
- (32) Thampy, A.; Darak, M.; Dhamodharan, S. Analysis Of Graphene Based Optically Transparent Patch Antenna For Terahertz Communications. *Physica E: Low-dimensional Systems and Nanostructures* **2015**, 66, 67-73.
- (33) Bala, R.; Marwaha, A. Development Of Computational Model For Tunable Characteristics Of Graphene Based Triangular Patch Antenna in THz Regime. *Journal of Computational Electronics* 2015, 15, 222-227.